Derivation of enhanced potentials for uranium dioxide and the calculation of lattice and intrinsic defect properties

Mark S.D. Read [a,*], Robert A. Jackson [b]

[a] AWE, Aldermaston, Reading, Berkshire RG7 4PR, United Kingdom
[b] Lennard-Jones Laboratories, School of Physical and Geographical Sciences Keele University, Keele, Staffordshire ST5 5BG, United Kingdom

ABSTRACT

Previously reported forms of the cation–anion Buckingham potential provide a significantly greater contribution than the repulsive Coulombic component at short-range thus predicting an unphysical attraction between the pair of ions. A detailed reappraisal of the computer modelling of uranium dioxide (UO_2) employing atomistic simulation techniques is presented. An improved set of interatomic potentials is derived in order to describe the lattice correctly under conditions subsequent to radiation damage with the creation of Frenkel pair defects.

Novel methodology is employed in the derivation of potentials ensuring applicability over the entire region of interest. The cation–anion potential is obtained *via* a combination of empirical fitting to crystal structural data and parametric fitting to additional physical properties. These potentials are subsequently verified and validated by calculation of additional bulk lattice properties, whose values agree favourably with those measured experimentally.

Atomistic computer simulation techniques are then used to investigate the defect properties of UO_2. The theoretical techniques are based upon efficient energy minimization procedures and Mott–Littleton methodology for accurate defect modelling and employed to calculate intrinsic defect formation energies and enable predictions of the expected type of intrinsic disorder to be made.

1. Introduction

Uranium dioxide (UO_2) has received renewed attention recently [1–3] following a nuclear renaissance driven by growing awareness of issues associated with CO_2 emissions, security of energy supply and waning fossil fuel reserves. Indeed, nuclear energy holds the promise to provide vast quantities of reliable baseline electricity at commercially competitive costs with modest environmental impact [4]. Interest in oxides as nuclear fuels, and in particular UO_2, began in the 1950s [5], with the introduction of UO_2 as a fuel in the BWR, PWR, CANDU and AGR reactor systems occurring during the following decade.

Currently, UO_2 is employed as the standard fuel in light water nuclear reactors due, in part, to its desirable properties which include: maintaining the fluorite structure over a wide temperature range up to a melting point of ≈3125 K, accommodating substantial quantities of fission products without significant perturbation of the lattice, maintaining these useful properties in a variety of environments and exhibiting chemical stability [6,2].

UO_2 is also of great technological importance in other arenas and improved understanding of the factors which can limit or induce uranium corrosion is of interest to a variety of industrial activities [7,8]. The extreme affinity of pure uranium for oxygen is well documented [9] with at least 16 oxides observed between UO_2 and UO_3 comprising the principal products of uranium metal corrosion [10]. Once formed as a layer on the surface of metallic uranium, the oxides act as a passive barrier to further corrosion. Thus, it is a generally accepted view that the reactivity of uranium towards various gases is affected primarily by the properties of its native oxide layer. For example, in the case of uranium–hydrogen systems, the surface oxide layer prevents rapid concentration of hydrogen at the metal surface and, as a result, provides a limiting influence on the onset of the gas–solid reaction that forms pyrophoric uranium hydride (UH_3).

Atomistic computer simulation techniques remain complementary to experimental methods and are ideally suited to provide fundamental insight into the defect chemistry. In view of the importance of UO_2, there remains a strong incentive for reliable theoretical studies. For this reason several initial derivations of interatomic potential models for UO_2 [11–13], and their application in the calculation of perfect and defect lattice properties, were conducted during the 1970s.

Indeed, seminal computational studies of UO_2 conducted in the 1980s [14–20] provide an erudite foundation for the current simulations. However, the premise upon which these computer simulation techniques are based, involves the specification of interatomic

* Corresponding author.
E-mail addresses: mark.read@awe.co.uk (M.S.D. Read), r.a.jackson@chem.keele.ac.uk (R.A. Jackson).

potential parameters. Modifications are required in order to describe the lattice correctly under conditions experienced subsequent to radiation damage with the creation of Frenkel pair defects: since reported forms of the cation–anion Buckingham potential provide a significantly greater contribution than the repulsive Coulombic component at short-range thus effecting an unphysical attraction between the pair of ions.

In addition, further understanding of the UO_2 system coupled with the more recent availability of experimental data and the benefit of increased computational resource (both in terms of improved hardware and enhanced simulation codes), have provided the impetus for improving the potentials reported previously by Jackson et al. [18]. Moreover, the methodology employed to derive the short-range pair potentials includes a novel approach to empirical fitting which explores the parametric surface to select values giving good accord with a wide range of observed data.

The present simulations of the UO_2 bulk are an informative preliminary to further research considering non-stoichiometry, substitutional defects, anion transport and diffusion mechanisms and more complex simulations of both bulk terminated and reconstructed surfaces, which are currently being undertaken. Prior to discussing the results of this study, the simulation approach employed is described in brief.

2. Computational techniques

2.1. Empirical potentials and calculation of lattice properties

The atomistic simulations presented here employ the same methodology for the treatment of perfect and defective lattices as employed in our previous studies of rare earth oxides [21] and fluorides [22]. The atomistic approach to modelling crystal structure and associated properties involves the definition of interatomic potential functions to simulate the forces acting between ions and expresses the total energy of the system as a function of atomic coordinates. For rare earth oxides, the calculations are commonly formulated within a Born model representation, with the total energy (E_{ij}) partitioned into long-range Coulombic interactions and a short-range analytical function ($\phi(r_{ij})$) to model interactions attributed to the repulsion between electron charge clouds, van der Waals attraction, etc. described by:

$$E_{ij} = \frac{q_i q_j}{r_{ij}} + \phi(r_{ij}) \tag{1}$$

where q_i and q_j represent *formal ionic charges* and r_{ij} the interatomic distance. The short-range interaction combines a number of components including non-bonded interactions (electron repulsion and van der Waals attraction) and electronic polarizability. A number of standard analytical functions are available for the non-bonded potential, but for ionic or partially ionic materials the most commonly used is the Buckingham form described by Eq. (2). The form of the Buckingham potential may be justified from a theoretical perspective since the repulsion between overlapping electron densities, due to the Pauli principle, takes an exponential form at reasonable distances.

$$\phi^{\text{Buckingham}}(r_{ij}) = \underbrace{A_{ij} \exp\left(-\frac{r_{ij}}{\rho_{ij}}\right)}_{\text{repulsive}} - \underbrace{\frac{C_{ij}}{r_{ij}^6}}_{\text{attractive}} \tag{2}$$

Eq. (2) contains a repulsive exponential and an attractive term with constants A, ρ and C obtained *via* empirical fitting [23]. Due to the rapid convergence of this short-range energy to zero, in order to improve the efficiency of the calculations, this interaction energy function does not contribute beyond a defined cut-off of 15 Å.

It is essential to include a description of the electronic polarization of ions in studies of defect energies to account for the polarization of neighbouring ions in the lattice surrounding charge defects (although these terms are less important in simulations purely of structural properties). Greatest success has been enjoyed by shell model descriptions of polarizability such as that of Dick and Overhauser [24] in which the development of an ionic dipole is described in simple mechanical terms of the displacement of a massless shell, representing the valence-shell electrons, relative to a core in which all the mass is concentrated, representing the nucleus shielded by the inner core electrons.

The ion charge is partitioned between the core and shell such that the sum of their charges is the total ion charge. Although convenient to think in terms of this physical picture, in certain situations the shell may carry a positive charge, particularly for metal cations. The core and shell are Coulombically screened from each other, but coupled by a harmonic spring of force constant k_{cs}. The polarizability of the ion (α) *in vacuo* is related to the shell charge, q_s and spring constant, k_{cs} by Eq. (3) and, despite its crudity, the model has proved successful in describing the dielectric and lattice dynamic properties of perfect and defective ionic materials.

$$\alpha = \frac{q_s^2}{k_{cs}} \tag{3}$$

By convention, the short-range forces are specified to act on the shell, while the Coulomb potential acts on both. Hence, the short-range forces act to damp the polarizability by effectively increasing the spring constant, and thus the polarizability is now environment dependent. The shell model has been widely adopted within the ionic materials community, particularly within the UK.

The interaction (E) between the core and the massless shell, on which all the pair potentials act, is embodied within the General Utility Lattice Program (GULP) [25–27] and considered to adopt the following form:

$$E = \frac{1}{2} k_2 r^2 + \frac{1}{24} k_4 r^4 \tag{4}$$

with r being the distance between the core and the shell, k_2 representing the harmonic spring constant with anharmonic contributions from k_4. k_4 terms are employed in certain instances to prevent unphysically large core-shell separations; however, only k_2 spring constants were required for this study with a maximum core-shell separation of 0.6 Å permitted.

Having derived suitable potentials, the lattice energy of the material is minimized by varying the structural parameters (atomic positions and lattice parameters). Values of lattice properties, such as elastic and dielectric constants, are calculated for the minimum energy structure. It should be stressed, as argued previously [28], that employing such a model does not necessarily mean that the electron distribution corresponds to a fully ionic system and that the general validity of the potential model is assessed primarily by its ability to reproduce observed crystal properties. In practice, it is found that models based on formal charges work well even for some semicovalent compounds such as silicates and zeolites.

2.2. Calculation of defect properties

An important feature of these calculations is the treatment of lattice relaxation about the point defect (or defect cluster). The celebrated Mott–Littleton approach [29,30] is to partition the crystal lattice surrounding the defect into two concentric spherical regions about a specified centre, usually considered to be the mid point of the perturbed lattice sites. In the inner sphere ($r \leqslant r_a$ – region I) the ions are strongly displaced by the presence of the defect so that the interactions are treated explicitly and species are allowed to relax fully. In contrast, more distant parts of the crystal lattice in the
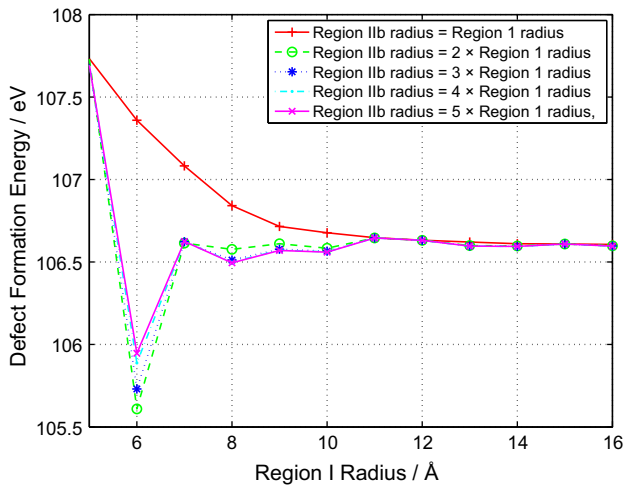
Fig. 1. Vacancy cluster defect energy as a function of size of region I.

outer region ($r > r_b$ – region IIb), where the defect forces are relatively weak, ions interact with any net charge on the defect and are treated implicitly as a dielectric continuum. In the region between the first and second sphere ($r_a < r \leqslant r_b$ – region IIa) ions are weakly perturbed leading to harmonic relaxations, this interface region ensures smooth convergence between explicitly summed and continuum regions.

In order to achieve the maximum degree of accuracy from the Mott–Littleton methodology, careful consideration of the region I and IIa radii is required. In order to determine the most appropriate cut-offs, the dependence of the calculated energy on the size of these regions was investigated. Results are summarized graphically in Fig. 1 for the case of a Schottky pair. It is observed that the optimal value for a region IIa radius is double that of region I as extending this interface region beyond this point has no significant increase in accuracy for a given region I size.

Fig. 1 demonstrates that convergence is achieved asymptotically with region I sizes above 11 Å and for calculations presented in this report, radii of 14 and 28 Å were used for regions I and IIa respectively, leading to $\approx$1600 ions in region I and $\approx$12,000 ions in region IIa as illustrated in Fig. 2. These perfect and defective lattice methods are embodied in the GULP code where the explicit simulation of the inner region employs efficient energy minimization methods which make use of first and second derivatives of the energy functions with respect to ion coordinates.

3. Results and discussion

Uranium metal is not observed to form a passivating oxide coating, but corrodes instead on prolonged exposure to air yielding a complex mixture of oxides: including UO_2, U_3O_8 and several polymorphs of the stoichiometric UO_3. The dioxide UO_2 adopts the fluorite structure but may incorporate interstitial oxygen anions to form the non stoichiometric series UO_{2+x}, $0 < x < 0.25$. In order to further the understanding of the role of the dioxide in limiting the diffusion of hydrogen from the surface to the underlying metal, a robust model of the UO_2 lattice is required. Prior to the derivation of suitable potentials that physically describe the system, experimental observations employed by the empirical fitting procedures are surveyed and a summary presented in the following subsection.

3.1. Experimental data

UO_2 adopts the fluorite structure [31] ($Fm\bar{3}m$), typical of ionic compounds, illustrated in Fig. 3. This may be considered as an fcc
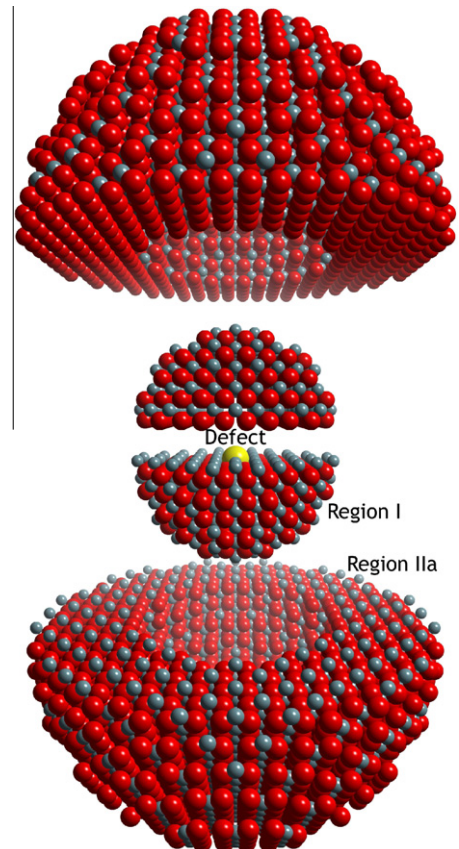

Fig. 2. Representation of the Mott–Littleton two region strategy for defect simulations.
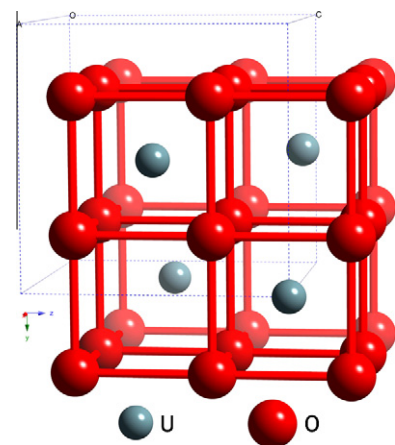

Fig. 3. Observed crystal structure of UO_2.

lattice with a lattice constant (a_0) of 5.4682 Å and a basis of a cation at the origin and anions at $\pm(\frac{1}{4}, \frac{1}{4}, \frac{1}{4})$.

In addition to the crystallographic data, elastic constants (C_{11}, C_{12} and C_{44}), static (ϵ_0) and high frequency (ϵ_∞) dielectric constants were employed during empirical fitting procedures; a summary of their experimental provenance is listed in Tables 1–3 in addition to other bulk properties for subsequent comparison and validation of the simulation.

3.2. Derivation of interatomic potentials

Govers et al. [1] provide an informative review of pair potentials development for UO_2. However, in order to describe post radiation

Table 1
Reported elastic constants for UO₂.

Reference	C_{11} (GPa)	C_{12} (GPa)	C_{44} (GPa)
Dolling et al. [32]	401 ± 9	108 ± 20	67 ± 6
Wachtman et al. [33]	396 ± 1.8	121 ± 1.9	64.1 ± 0.17
Fritz [34]	389.3 ± 1.7	118.7 ± 1.7	59.7 ± 0.3

Table 2
Reported dielectric constants for UO₂.

	Dielectric constants	
Reference	Static ϵ_0	High frequency ϵ_∞
Dolling et al. [32]	24	5.3
Schoenes [35]	21.5 ± 1	5 ± 0.05

Table 3
Reported bulk properties for UO₂.

	Moduli			Poisson's
Reference	Bulk K (GPa)	Shear G (GPa)	Young's E (GPa)	Ratio ν –
Wachtman et al. [33]	213.0	87.0	231.0	0.319
Padel et al. [36]	183.4	75.0	204.7	0.314
Marlowe [37]	203.2	82.1	217.2	0.323
Fritz [34]	209.0	83.0	221.0	0.324

damaged UO₂ accurately, unphysical attractive forces at short-range effected by positive C terms for the Buckingham form require negating. For the anion–anion potential this is achieved by employing the 'Buckingham four range' function which discards the attractive $-C/r^6$ term below a certain distance, derived and employed successfully by Jackson et al. [18] in their studies of UO₂.

For the cation–anion potential, this functional form is inappropriate and thus a potential is derived of the Born–Mayer form which does not include the attractive r^{-6} term. A novel approach to deriving these parameters from the available experimental data is described which explores the parametric surface to select values giving good accord with a wide range of observed data.

3.2.1. Anion–anion potentials

The 'Busker' $O^{2-} \cdots O^{2-}$ potential [38] illustrates the limitations of incorporating an attractive r^{-6} term. Fig. 4 plots the energy of this potential as a function of interatomic distance which is clearly seen to become catastrophically and unphysically attractive when the anions are separated by less than 0.75 Å.

Thus, use of a potential of this form is inadequate in simulating anion transport or oxygen Frenkel pairs. The case of an oxygen interstitial (O_i'') occupying the $(\frac{1}{2}, \frac{3}{4}, \frac{3}{4})$ position illustrates this point in Fig. 5. The 'relaxed' coordinates do not reach a minimum energy configuration and the lattice occupies an unphysical state.

This phenomenon may be avoided by employing a 'Buckingham four range' potential reported by Jackson et al. [18] for UO₂ and used subsequently by Vessal et al. [39,40] in the simulation of silica. Here, only the most appropriate terms of the Buckingham function are used over the relevant interatomic distance as the function is defined by intervals shown by Eq. (5).

$$\phi^{\text{Buck4}}(r_{ij}) = \begin{cases} A_{ij} \exp\left(-\frac{r_{ij}}{\rho_{ij}}\right) & \text{if } r_{\min} < r_{ij} \leqslant \text{cut}_1 \\ \sum_{m=0}^{5} a_m\, r_{ij}^m & \text{if } \text{cut}_1 < r_{ij} \leqslant r_{\min} \\ \sum_{n=0}^{3} b_n\, r_{ij}^n & \text{if } r_{\min} < r_{ij} \leqslant \text{cut}_2 \\ -\frac{C_{ij}}{r_{ij}^6} & \text{if } \text{cut}_2 < r_{ij} \leqslant r_{\max} \end{cases} \quad (5)$$
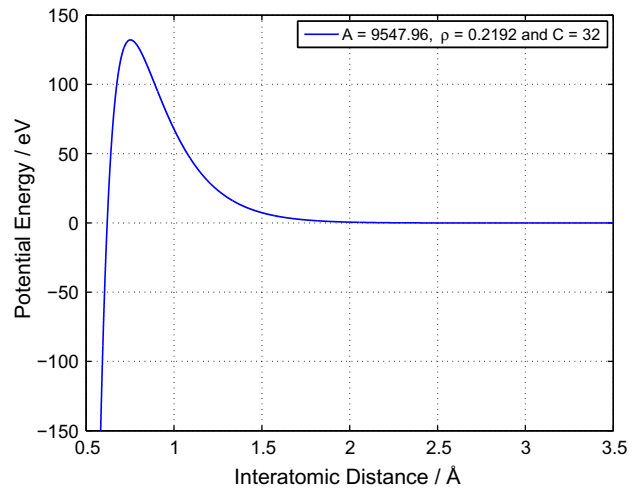
Fig. 4. Plot of the Busker $O^{2-} \cdots O^{2-}$ Buckingham potential.

(a) Unrelaxed   (b) Relaxed
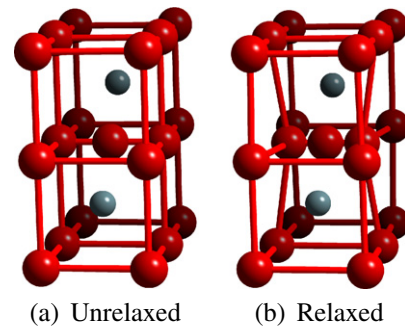
Fig. 5. Unrelaxed (a) and relaxed (b) UO₂ lattice surrounding O_i''.

Table 4
Lattice potential for $O^{2-} \cdots O^{2-}$ (Buckingham four range form).

Interaction	Short-range parameters			Shell model[a]	
	A eV	ρ Å	C eV Å⁶	Y |e|	k_2 eV Å⁻²
$O^{2-} \cdots O^{2-}$ [b]	11,272.6	0.1363	134.0	−4.4	296.2
	$r_{\min}$ Å	cut₁ Å	$r_{\min}$ Å	cut₂ Å	$r_{\max}$ Å
	0.0	1.2	2.1	2.6	15.0

[a] Y and k_2 are the shell charge and spring constant respectively.
[b] Ref. [18].

where $r_{\max}$ is the short-range cut-off. The potential is subjected to the constraint that the functions and their first and second derivatives must be continuous at the boundary points (cut₁ and cut₂) and also that the function possess a stationary point at $r_{\min}$ which must be a minimum. Values for the required parameters derived by Jackson et al. are listed in Table 4 and used subsequently in this study.

Constants for the polynomials (of order i) are calculated by the spline fitting procedure embodied within the GULP code. The function is splined at cut₁, $r_{\min}$ and cut₂ so that the energy, and first and second derivatives, are continuous using formulae shown in Eqs. (6)–(8). The function has a stationary point at $r_{\min}$ occurring when the first derivative of the function equals zero. For a minimum, the second derivative must be greater than zero as illustrated in Eq. (9):

$$E(r) = \sum_{m=0}^{i} a_m \, r^m \qquad (6)$$

$$\frac{dE}{dr} = \sum_{m=1}^{i} m a_m \, r^{m-1} \qquad (7)$$

$$\frac{d^2E}{dr^2} = \sum_{m=2}^{i} m \cdot (m-1) a_m \, r^{m-2} \qquad (8)$$

for a minimum, $\qquad \dfrac{dE}{dr} = 0 \quad$ and $\quad \dfrac{d^2E}{dr^2} > 0 \qquad (9)$

The full contiguous function is illustrated in Fig. 6; due to the continuous repulsive nature at short distances this interatomic potential describes the perturbation of the lattice surrounding the O_i'' occupying the $(\frac{1}{2}, \frac{3}{4}, \frac{3}{4})$ position correctly as illustrated in Fig. 7, minimizing the atomic coordinates and predicting a point defect energy of -9.53 eV. Thus proving the robust nature and suitability of this form for subsequent simulations of the radiation damaged lattice.

3.2.2. Cation–anion potentials

The Buckingham four range form is not applicable to the cation–anion interaction due to the absence of a stationary point in the function; thus the corresponding (standard) Buckingham form reported by Jackson et al. [18] listed in Table 5 was investigated initially for $U^{4+} \cdots O^{2-}$ interactions.

For the same reasons discussed previously when considering anion–anion interactions, the presence of a positive C term causes unphysical and catastrophic attraction when the ions are in close proximity, in this instance closer than 1.1 Å. This phenomenon is
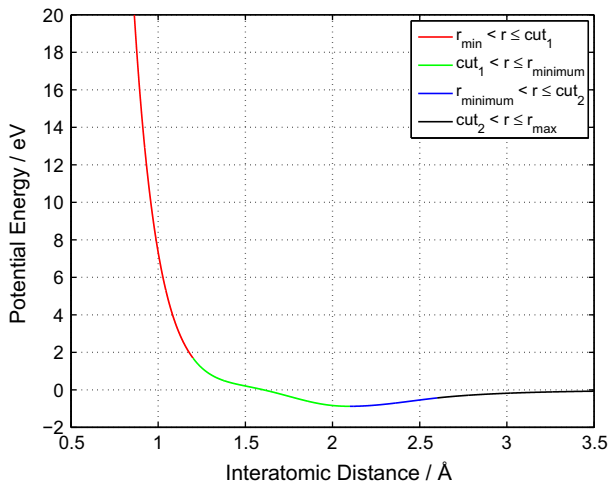
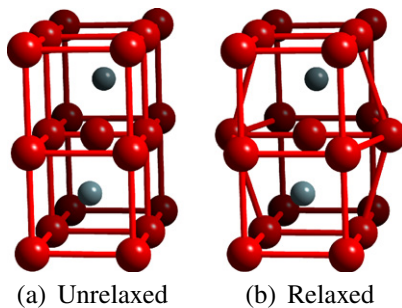**Fig. 6.** Plot of the $O^{2-} \cdots O^{2-}$ Buckingham four range potential.

Fig. 7. Unrelaxed (a) and relaxed (b) UO₂ lattice surrounding O_i''.

Table 5
Lattice potential for $U^{4+} \cdots O^{2-}$ (Buckingham form).

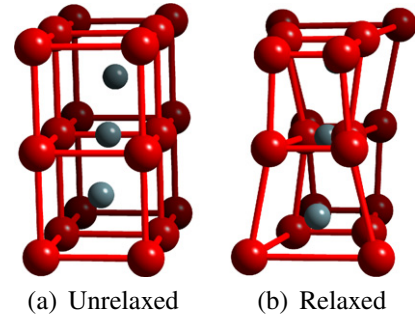| Interaction	Short-range parameters			Shell model	
	A	ρ	C	Y	k_2
	eV	Å	eV Å⁶	$|e|$	eV Å⁻²
$U^{4+} \cdots O^{2-a}$	1518.92	0.38208	65.41	6.54	94.24

[a] Ref. [18].

Fig. 8. Unrelaxed (a) and relaxed (b) UO₂ lattice surrounding $U_i^{\cdots}$.

illustrated by employing this potential and placing a uranium interstitial ($U_i^{\cdots}$) at the $(\frac{1}{2}, \frac{3}{4}, \frac{3}{4})$ position. The result is shown in Fig. 8 when the simulation fails to reach a minimum due to the collapse of the lattice in on the (attractive) uranium interstitial ion.

To solve this issue, a novel cation–anion potential is derived in which the C parameter is considered to be zero, thus representing a function the Born–Mayer form. By judicious selection of a pair of A and ρ parameters which take account of and incorporate the attractive nature of the excluded ($-C/r^6$) term, a robust potential will describe the cation–anion interaction over the entire region of interest.

GULP has enjoyed much success in deriving potentials using empirical fitting algorithms embodied within the code: selected parameters may be adjusted systematically (usually via a least squares fitting technique) until optimal agreement is obtained between predicted and observed properties (such as structural and lattice properties). However, a global minimum is not guaranteed and in practice the results obtained by this method appear sensitive to the initial starting configuration.

Thus to understand further the form and behaviour of the cation–anion parameters, a novel procedure was developed to survey the potential landscape and select appropriate values for the A and ρ parameters in a sequential manner. The initial stage of this process involves screening a range of A and ρ values and observing the discrepancy between predicted and observed structural properties. Fig. 9 illustrates the potential surface by plotting the difference between predicted and observed UO₂ lattice constant (a_0) for a range of A (750–2200 eV) and ρ (0.2–0.5 Å) values. The surface mesh is interpolated to obtain combinations which reproduce a_0 exactly (i.e., where $\delta = 0$) as indicated by red lozenge markers.

It is of interest to note that within this selected range there is a multitude pairs of values which reproduce the crystal structure. However, a pair which also describe the physical characteristics of the lattice are required for a reliable and robust model. Thus, elastic constants predicted from this solution set are investigated subsequently.

Elastic constants represent the second derivatives of the energy density with respect to strain:

$$C_{ij} = \frac{1}{V} \left(\frac{\partial^2 U}{\partial \epsilon_i \partial \epsilon_j} \right)$$
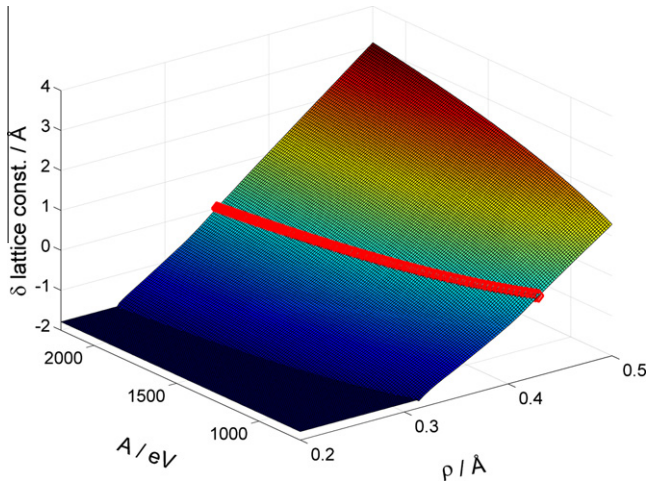
Fig. 9. Plot of the difference between predicted and observed UO$_2$ lattice constant for A and ρ values of the U$^{4+} \cdots$ O^{2-} Born–Mayer potential.

thereby describing the mechanical hardness of the material with respect to deformation. Since there are six possible strains within the notation scheme, the elastic constant tensor within GULP is a 6×6 symmetric matrix. The 21 potentially independent matrix elements are usually reduced considerably by symmetry, *e.g.* C_{11}, C_{12} and C_{44} being unique elements for cubic UO$_2$.

Employing the solution set identified in Fig. 9, predicted elastic constants are plotted as a function of the A parameter as illustrated in Fig. 10.

Here the observed values for C_{11}, C_{12} and C_{44} reported by Fritz [34], indicated by black circles, are used to determine a suitable and representative value for the A parameter. The corresponding ρ parameter value reproducing a_0 is obtained subsequently from interpolation of the solution set shown in Fig. 9.

The importance of the shell model, discussed earlier, to account for polarization during calculation of defect energies in polar crystals is highlighted by Catlow [12]: "Owing to its high dielectric constant, UO$_2$ illustrates in a particularly marked manner, the problems encountered when calculating defect energies in polar crystals". Several examples quoted within this paper demonstrate the requisite use of the shell model of Dick and Overhauser in defect studies which correctly simulates both elastic and dielectric properties; an essential requirement for reliable calculations of de-
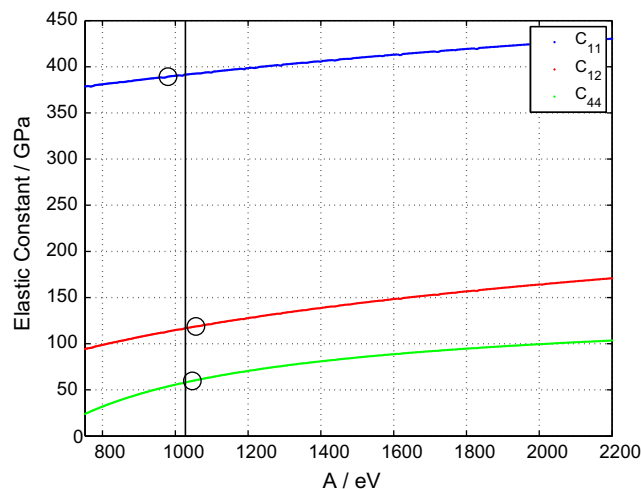
fect energies. Thus, the final stage is to derive a spring constant (k_2) for the cation by empirical fitting to observed dielectric properties.

Dielectric properties are of crucial importance in many contexts, including those beyond the strictly bulk properties. For example, the response of a solid to a charged defect depends on the inverse of the dielectric constant. The actual value of the dielectric constant varies according to the frequency of the electromagnetic field applied. Commonly two extreme values are quoted, namely the static (ϵ_0) and high frequency (ϵ_∞) dielectric constants. In the static limit all degrees of freedom of the crystal, both nuclear and electronic, are able to respond to the electric field and therefore to provide screening. At the high frequency limit the oscillation is greater than the maximum vibrational frequency of the material and therefore only the electrons are able to respond to the perturbation fast enough.

Embodied within GULP, the static dielectric constant tensor can be determined from the Cartesian second derivative matrix of all particles, $D_{\alpha\beta}$, and the vector, q, containing the charges of all particles:

$$\varepsilon_{\alpha\beta}^0 = \delta_{\alpha\beta} + \frac{4\pi}{V}\left(qD_{\alpha\beta}^{-1}q\right)$$

The expression for the high frequency dielectric constant is identical to that for the static equivalent, except that the second derivative matrix, $D_{\alpha\beta}$, now only includes the Cartesian components for any shells present within the model. If a core only model is being used then the high frequency dielectric tensor is just a unit matrix. Hence information regarding the high frequency dielectric constants is particularly useful in determining the parameters of a shell model due to the relatively direct correlation.

Because the dielectric constant tensor depends on the inverse second derivative matrix, it has many of the characteristics of the Hessian matrix and is therefore quite a sensitive indicator of whether a potential model is sensible. Extreme values, particularly negative ones, instantly point to the fact that the potential model is inadequate or that the system wishes to undergo a symmetry change.

Fig. 11 illustrates a plot of the predicted zero and high frequency dielectric constants as a function of spring constant (k_2), with reported values from Schoenes [35] superimposed. A value for the spring constant is selected to provide optimal agreement with both dielectric constants.

Values obtained from the above procedure are listed in Table 6.

Prior to assessing the applicability of these Born–Mayer parameters, the form of the potential function is compared to that of the
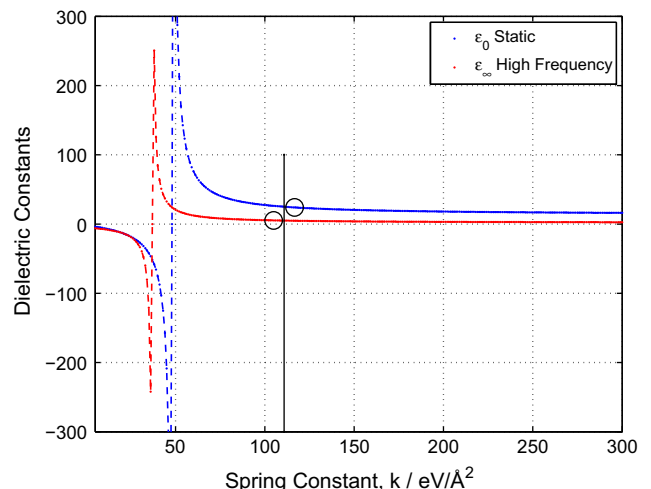

Fig. 10. Plot of elastic constants as a function of the A parameter.

Fig. 11. Plot of dielectric constants as a function of the spring, k_2, parameter.

Table 6
Lattice potential for $U^{4+} \cdots O^{2-}$ (Born–Mayer form).

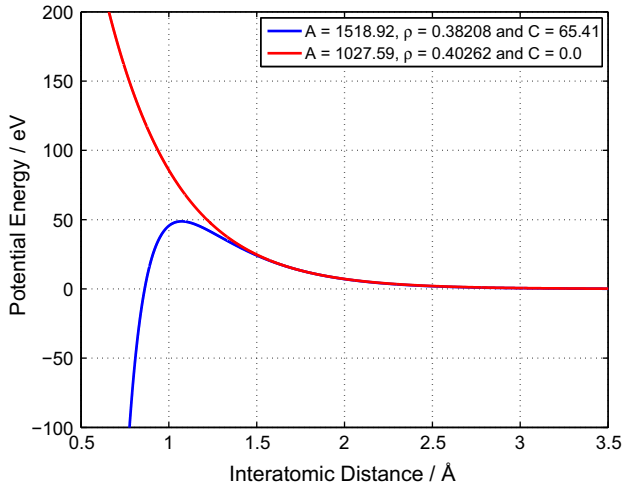| Interaction	Short-range parameters		Shell model	
	A	ρ	Y	k_2
	c eV	Å	$|e|$	eV Å^{-2}
$U^{4+} \cdots O^{2-}$	1027.5967	0.402616	6.54	110.75343

Fig. 12. Comparison between parameters for $U^{4+} \cdots O^{2-}$ potential.

Jackson Buckingham type. Fig. 12 shows both functions being in accord from separation distances greater than 1.5 Å; thus confirming that the Born–Mayer form compensates for the loss of the attractive C parameter over this range. Moreover, when the pair of ions approach each other at separations less than 1.5 Å, the Born–Mayer form (red line) continues to describe a repulsive interaction, unlike the Buckingham form where catastrophic attraction begins to occur at 1.0 Å.

Applying this Born–Mayer $U^{4+} \cdots O^{2-}$ potential to the previous consideration of a uranium interstitial ($U_i^{\cdots}$) at the $(\frac{1}{2}, \frac{3}{4}, \frac{3}{4})$ position results in convergence of the defect calculation predicting realistic expansion of the oxygen sub-lattice to accommodate the interstitial as illustrated in Fig. 13.

Thus, a set of potentials which describe the UO$_2$ system and continue to perform successfully under conditions of radiation damage have been derived. The anion–anion Buckingham potential listed in Table 4 is employed in conjunction with the cation–anion Born–Mayer potential (Table 6).
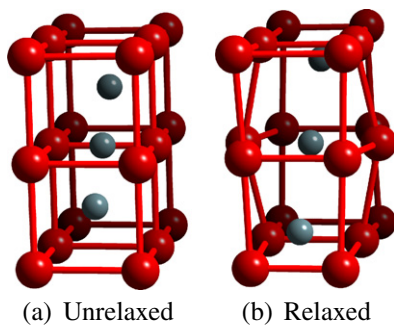

(a) Unrelaxed   (b) Relaxed

Fig. 13. Unrelaxed (a) and relaxed (b) UO$_2$ lattice surrounding $U_i^{\cdots}$.

3.3. Perfect lattice properties

The applicability of the model, and validation of potentials upon which it is based, is assessed by comparison of predicted properties of the perfect lattice to experimentally observed values. Table 7 shows excellent agreement between calculated parameters and reported crystallographic structure, elastic constants and static and high frequency dielectric constants.

However, the ability of the potentials to reproduce these parameters accurately is unsurprising since they were all employed at various stages of the empirical fitting procedure. To validate the model further, other properties are considered and prediction compared once more to reported observation.

3.3.1. Mechanical properties

Bulk (K) and shear (G) moduli contain information pertaining to the hardness of a material with respect to various types of deformation and are much more facile to determine experimentally than the elastic constant tensor. Considering the response of a material as a function of applied isotropic pressure, an equation of state can be fitted to a plot of pressure versus volume with the bulk modulus comprising one of the curve parameters: typically, a third or fourth order Birch–Murgnahan equation of state is employed. In addition, bulk and shear moduli are related to the elements of the elastic constant. However, since there is no unique definition of this transformation, that of Voight is employed in this study:

$$K_{Voight} = \frac{1}{9}(C_{11} + C_{22} + C_{33} + 2(C_{12} + C_{13} + C_{23})) \quad (10)$$

$$G_{Voight} = \frac{1}{15}[C_{11} + C_{22} + C_{33} + 3(C_{44} + C_{55} + C_{66}) - C_{12} - C_{13} - C_{23}] \quad (11)$$

For a cubic system, symmetry provides the following equivalent terms:

$$C_{11} \equiv C_{22} \equiv C_{33} \quad (12)$$
$$C_{44} \equiv C_{55} \equiv C_{66} \quad (13)$$
$$C_{12} \equiv C_{13} \equiv C_{23} \quad (14)$$

Thus, for the isotropic cubic crystal of UO$_2$, bulk and shear moduli are defined by the simplified relationships Eqs. (15) and (16) respectively.

$$K = \frac{1}{3}(C_{11} + 2C_{12}) \quad (15)$$

$$G = \frac{1}{15}(3C_{11} + 9C_{44} - 3C_{12}) \quad (16)$$

Subsequent to the calculation of K and G, Young's modulus and Poisson's ratio may be determined. Indeed, for homogeneous isotropic materials, simple relationships enable bulk (K), shear (G) and Young's (E) moduli, in addition to Poisson's ratio (ν), to be determined provided at least two of the terms are known [41].

Application of uniaxial tension to a material effects a lengthening which can be measured according to the strain. The ratio of stress to strain defines the value of the Young's modulus (E) for that axis:

$$E_\alpha = \frac{\sigma_{\alpha\alpha}}{\epsilon_{\alpha\alpha}} \quad (17)$$

Since materials tend to increase in length under tension, values of this quantity are typically positive. As K and G are known, E may be calculated by the following equation:

$$E = \frac{9KG}{3K + G} \quad (18)$$

Complementary to Young's modulus, the Poisson ratio (v) measures the change in a material at right angles to the uniaxial stress. Formally defined as the ratio of lateral to longitudinal strain under a uniform, uniaxial stress; assuming an isotropic medium, the following expression is used to calculate this property:

$$v_\alpha(\beta) = -S_{\alpha\alpha\beta\beta}Y_\beta \tag{19}$$

Poisson's ratio is usually positive (since most materials naturally shrink orthogonal to an applied tension) with typical values for many materials lying in the range 0.2–0.3, below the theoretical maximum of 0.5. As with Young's modulus, Poisson's ratio may also be determined from K and G by the following equation:

$$v = \frac{3K - 2G}{2(3K + G)} \tag{20}$$

Acoustic velocities are key quantities in the interpretation of seismic data. The polycrystalline averages of these acoustic velocities in a solid can be derived from the bulk and shear moduli of the material, as well as the density, ρ. There are two values, that for a transverse wave, V_s and that for a longitudinal wave, V_p, which are given by the following equations:

$$V_s = \sqrt{\frac{G}{\rho}} \tag{21}$$

$$V_p = \sqrt{\frac{4G + 3K}{3\rho}} \tag{22}$$

Employing calculated elastic constants listed in Table 7, mechanical properties of the perfect bulk are predicted using the above relationships: listed in Table 8, these parameters agree favourably with those calculated from the elastic constants reported by Fritz [34] in Table 1 and his reported values listed in Table 3.

To enable direct comparison with observation, bulk properties listed in Table 8 were derived from elastic constants; although good accord is observed with other reported values (Table 9). However, in practice, these mechanical properties are obtained directly from algorithms embodied within GULP: Subsequent to the determination of the optimized structure for a material, a wide range of physical properties may be calculated based on the curvature of the energy surface about the minimum which include both mechanical properties, such as the bulk modulus and elastic constants, as well as dielectric properties.

3.3.2. Phonon modes

It is of interest, and also important in the further validation of the potentials, to observe the degree to which other bulk lattice properties may be calculated by the model. The phonon spectrum has been measured at room temperature by Dolling et al. [32] and

Table 7
Comparison of predicted and observed properties of UO$_2$.

Property	Units	Calculated	Observed	Δ (%)
Lattice constant				
(a_0)	Å	5.4682	5.4682	0.0
$U^{4+} \cdots U^{4+}$ separation	Å	3.8666	3.8666	0.0
$U^{4+} \cdots O^{2-}$ separation	Å	2.3678	2.3678	0.0
$O^{2-} \cdots O^{2-}$ separation	Å	2.7341	2.7341	0.0
C_{11}	GPa	391.4	389.3	0.5
C_{12}	GPa	116.7	118.7	−1.7
C_{44}	GPa	58.1	59.7	−2.7
Dielectric constants				
Static		24.8	24.0	3.3
High frequency		5.0	5.3	−5.7

Table 8
Calculated bulk properties for UO$_2$.

Reference	Moduli		
	Bulk K (GPa)	Shear G (GPa)	Young's E (GPa)
Fritz [34][a]	208.9 ± 1.7	89.94 ± 0.2	236.0 ± 0.7
Calculated[b]	208.29	89.80	235.54
Reference	**Poisson's ratio**	**Velocity**	
		S-wave V_s (km/s)	P-wave V_p (km/s)
	v –		
Fritz [34][a]	0.3117 ± 0.001	–	–
Calculated[b]	0.3115	9.04758	17.29242

[a] Calculated from reported elastic constants.
[b] Calculated from elastic constants listed in Table 7.

Table 9
Reported bulk properties for UO$_2$.

Reference	Moduli			Poisson's
	Bulk K (GPa)	Shear G (GPa)	Young's E (GPa)	ratio v –
Wachtman et al. [33]	213.0	87.0	231.0	0.319
Padel et al. [36]	183.4	75.0	204.7	0.314
Marlowe [37]	203.2	82.1	217.2	0.323
Fritz [34]	209.0	83.0	221.0	0.324
Calculated	208.29	89.80	235.54	0.3115

comparison to the calculated phonon dispersion curves (at 0 K) is shown in Fig. 14.

Fig. 14 shows the measured dispersion curves for the symmetric directions [0 0 ξ], [ξ ξ 0] and [ξ ξ ξ], or, in group-theory notation[1], Δ, Σ and Λ. It is of interest to note that whilst excellent agreement is observed with the majority of the acoustic and optical modes, calculations for branches exhibiting a temperature dependence consistently have lower wavenumber commensurate with the temperature difference between the two data sets.

In agreement with observations reported by Dolling et al., the model predicts triply degenerate representations corresponding to the acoustic modes (244.18 cm^{-1}); the lifting of the degeneracy by macroscopic electric field associated with the longitudinal optic modes (543.46 cm^{-1}) and the irreducible representation (ω_R) corresponding to a triply degenerate mode with the oxygen ions vibrating in antiphase (416.58 cm^{-1}).

The accurate prediction of phonon dispersion curves using atomistic simulation is dependent upon the spring constants of both ion species. Further discussion on the role of the shell model in calculating phonon frequencies is reported elsewhere [24,42,43]. However, since the overall agreement and trends are both very reasonable and certainly commensurate with that reported by Jackson et al. [18], the validity of the derived spring constants, to which phonon calculations are sensitive, is demonstrated.

Crystals with the fluorite structure possess a simple vibrational spectrum, here UO$_2$ exhibits one infrared active phonon with T_{1u} symmetry and, at long wavelengths ($k = 0$), a single Raman-active phonon of T_{2g} symmetry. The long wavelength mode comprises each atomic sub-lattice in relative motion (U–O stretching) and as such is triply degenerate. The calculated frequencies of some selected normal modes are given in Table 10 and compared to measured frequencies reported in the literature.

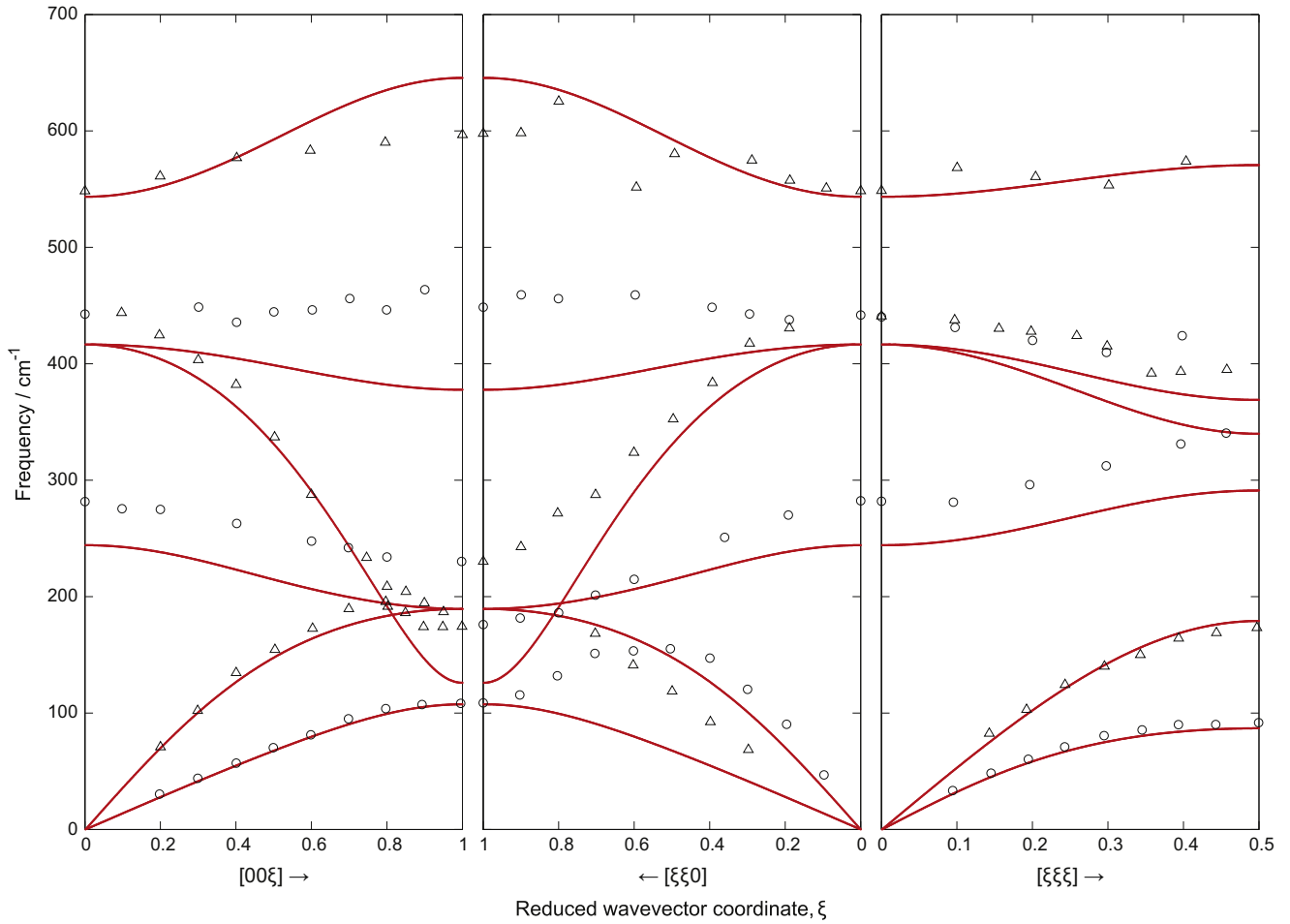[1] Described in further detail by Dolling et al. [32]

Fig. 14. Comparison of measured phonon dispersion curves for UO$_2$ at 296 K in three directions of high symmetry (open circles and triangles) using neutron scattering techniques reported by Dolling et al. [32] to calculated dispersion curves (red lines) based on derived potentials. (For interpretation of the references to colour in this figure legend, the reader is referred to the web version of this article.)

Table 10
Phonon frequencies for UO$_2$ derived from optical spectroscopy and comparison with calculated.

	Infra red (T_{1u})		Raman (T_{2g})
Reference	ω_{TO} (cm^{-1})	ω_{LO} (cm^{-1})	ω_R (cm^{-1})
Schoenes [35]	280 ± 2	578 ± 2	–
Axe and Pettit [44]	278 ± 2	556 ± 4	–
Dolling et al. [32]	284 ± 4	557 ± 20	447 ± 5
Calculated	244.18	543.46	416.58

Table 11
Calculated formation energies of isolated atomic defects.

Type of defect	Position	Formation energy (eV)
U^{4+} Vacancy (V$_U''''$)	(0,0,0)	78.12
O^{2-} Vacancy (V$_O^{\cdot\cdot}$)	$(\frac{1}{4},\frac{1}{4},\frac{1}{4})$	16.14
U^{4+} Interstitial (U$_i^{\cdot\cdot\cdot\cdot}$)	$(\frac{1}{2},\frac{1}{2},\frac{1}{2})$	−60.91
O^{2-} Interstitial (O$_i''$)	$(\frac{1}{2},\frac{1}{2},\frac{1}{2})$	−11.52

Region I comprises 1600 ions.

The initial slopes of the acoustic branches are consistent with independent measurements of the elastic constants [32–34] and the frequencies of the Transverse Optical (ω_{TO}) and Longitudinal Optical (ω_{LO}) modes at $q = 0$ are consistent with the measured static and high frequency [32,35] dielectric constants (ϵ_0 and ϵ_∞ respectively) through the Lyddane–Sachs–Teller relation [45]:

$$\left(\frac{\omega_{LO}}{\omega_{TO}}\right)^2_{q=0} = \frac{\epsilon_0}{\epsilon_\infty} \tag{23}$$

3.4. Defect properties and intrinsic defect behaviour

Calculations were performed first on the energies of isolated point defects (vacancies and interstitials) which are given in Table 11. In all cases, the lattice ions surrounding the defect are allowed

to relax in the energy minimization procedure using the previously described Mott–Littleton procedure. Calculated values for defect formation energies are compared with experimental observation reported in the literature [46–52].

3.4.1. Frenkel and Schottky energies

Individual point defect energies are combined to predict Frenkel and Schottky disorder formation energies (reported in Table 14). Frenkel defects can be represented by the following reactions employing Kröger–Vink notation [53]:

$$U_U^\times \rightleftharpoons V_U'''' + U_i^{\cdot\cdot\cdot\cdot} \tag{24}$$

$$O_O^\times \rightleftharpoons V_O^{\cdot\cdot} + O_i'' \tag{25}$$

Similarly, the Schottky defect can be expressed as:

Table 12
Calculated energies of oxygen Frenkel pair defects.

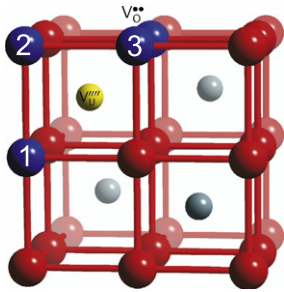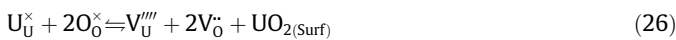| Type of defect	$V_O^{\cdot\cdot}$ position	O_i'' position	Formation energy (eV/defect)	Binding energy (eV/defect)
OFP 1	$\left(-\frac{1}{4},-\frac{1}{4},-\frac{1}{4}\right)$	$\left(\frac{1}{2},\frac{1}{2},\frac{1}{2}\right)$	1.62	−0.69
OFP 2	$\left(-\frac{1}{4},-\frac{1}{4},\frac{1}{4}\right)$	$\left(\frac{1}{2},\frac{1}{2},\frac{1}{2}\right)$	1.90	−0.41

Fig. 15. Lattice positions of uranium and oxygen vacancies associated with the Schottky defect, with the three possible sites for the second oxygen vacancy labelled.

$$U_U^\times + 2O_O^\times \rightleftharpoons V_U'''' + 2V_O^{\cdot\cdot} + UO_{2(Surf)} \qquad (26)$$

However, calculating formation energies in this manner assumes infinite dilution and omits the binding energy associated with the aggregation of point defects required to be taken into account in order for comparison to experimental observation. The following cluster calculations address this issue.

3.4.2. Frenkel pair clusters

Formation energies of oxygen and uranium Frenkel Pairs at infinite distance are predicted to be higher than those observed by experiment. Thus, in order to compare to reported data, defect clusters are simulated and the binding energy determined as the difference in energy between the cluster and its constituent point defects at infinite dilution.

For simulations where the oxygen interstitial is placed in close proximity to the vacancy, recombination is observed to occur during the geometry optimization procedure unless the oxygen interstitial is constrained. Thus, in order to calculate a cluster energy the oxygen defects were separated by a (lattice) uranium ion to prevent recombination. Two geometries for the Oxygen Frenkel pair (OFP) were considered and the respective coordinates and resulting energies are listed in Table 12.

3.4.3. Schottky defect clusters

In a similar manner, three configurations for the ion vacancies associated with the Schottky Defect were simulated. With an initial uranium vacancy at $(0,0,0)$ and the first oxygen vacancy at $\left(\frac{1}{4},\frac{1}{4},\frac{1}{4}\right)$, the second oxygen vacancy required to preserve charge neutrality was considered at (i) $\left(-\frac{1}{4},-\frac{1}{4},-\frac{1}{4}\right)$ (Sch. 1), (ii) $\left(-\frac{1}{4},+\frac{1}{4},-\frac{1}{4}\right)$ (Sch. 2) and (iii) $\left(-\frac{1}{4},+\frac{1}{4},+\frac{1}{4}\right)$ (Sch. 3) as illustrated in Fig. 15.

Defect formation energies for the three types of vacancy cluster associated with the Schottky defect are listed in Table 13. The most energetically favourable position for the second oxygen vacancy is predicted to be in Sch. 2 configuration and this cluster energy is combined with the associated energy of forming UO_2 at the surface to predict the Schottky defect energy listed in Table 14.

The predicted defect energies listed in Table 14, once allowing for the associated binding energy, are in good agreement with measured experimental values providing further evidence for the suitability of the potential set.

Table 13
Calculated formation energies of U^{4+} and O^{2-} pair defect clusters.

Type of defect	Second $V_O^{\cdot\cdot}$ position	Formation energy (eV/defect)	Binding energy (eV/defect)
Sch. 1	$\left(-\frac{1}{4},-\frac{1}{4},-\frac{1}{4}\right)$	35.60	−1.20
Sch. 2	$\left(-\frac{1}{4},+\frac{1}{4},-\frac{1}{4}\right)$	35.57	−1.23
Sch. 3	$\left(-\frac{1}{4},+\frac{1}{4},+\frac{1}{4}\right)$	35.80	−1.00

Table 14
Calculated energies of ionic defect clusters.

Type of defect	Formation energy		
	Infinite dilution (eV/defect)	Defect cluster (eV/defect)	Experimental observation (eV/defect)
Uranium Frenkel pair	8.15	6.17	4.75–6.3
Oxygen Frenkel pair	2.19	1.62–1.90	1.55–2.7
Schottky defect	2.62	1.50	2.00–2.3

Region I comprises 1746 ions.

4. Conclusions

The present study has illustrated the importance of a robust procedure in the derivation of interatomic pair potentials and that they need to be applicable to the complete range of interest of concern to post radiation damaged systems. Furthermore, by employing atomistic computer simulation techniques, intrinsic defects inherent in UO_2 that contribute to key solid state properties are able to be investigated. The report has drawn attention to the following main features:

Starting from a solution set of parameters which reproduce the crystallographic structure correctly, values are selected based in their ability to reproduce additional physical aspects of the lattice (*e.g.* elastic and dielectric constants).

A thorough understanding of the potential form and behaviour of constituent variables is paramount to their effective use in describing interatomic forces operating at separation distances applicable to radiation damaged material.

Additional bulk material properties (*e.g.* bulk, shear and Young's moduli and Poisson's ratio) calculated using the derived potentials are in good agreement with experimental observation.

The harmonic spring constant employed by the shell model (fitted to observed dielectric constants) reproduces the phonon dispersion curves at frequencies in reasonable agreement with those reported in the literature.

Subsequent to the validation of potentials using the pure lattice, calculated energies of intrinsic point and cluster defects are used to predict Frenkel and Schottky energies which lie within the range of those observed by experiment.

Schottky defects and Oxygen Frenkel pairs are calculated to be the most energetically preferred form of intrinsic defects.

5. Future work

The methodology described within this report has proven to be applicable to the derivation of interatomic pair potentials for acti-

nide oxides. Having proven the ability of these potentials to describe the bulk lattice of UO_2, the next logical stage will be to perform bulk terminated surface simulations to assess the transferability of the potentials and to recalculate the intrinsic defect energies to predict whether they are thermodynamically more stable dissolved in the bulk or at specific surfaces.

Once a comprehensive suite of static calculations has been completed, the potentials will be employed in molecular dynamic simulations which will provide a fundamental mechanistic insight into anion transport mechanisms and activation energies over a range of temperatures in order to derive diffusion coefficients from Arrhenius plots.

The combination of atomistic simulations provides access to the scale and temperature domains required to provide fundamental parameters which will underpin higher level constitutive models which predict the kinetics of materials ageing.

Acknowledgements

References

[1] K. Govers, S. Lemehov, M. Hou, M. Verwerft, J. Nucl. Mater. 366 (1–2) (2007) 161, doi:10.1016/j.jnucmat.2006.12.070.
[2] P. Nerikar, T. Watanabe, J.S. Tulenko, S.R. Phillpot, S.B. Sinnott, J. Nucl. Mater. 384 (1) (2009) 61, doi:10.1016/j.jnucmat.2008.10.003.
[3] D.A. Andersson, T. Watanabe, C. Deo, B.P. Uberuaga, Phys. Rev. B 80(6). doi:10.1103/PhysRevB.80.060101.
[4] Y. Guerin, G.S. Was, S.J. Zinkle, MRS Bull. 34 (1) (2009) 10.
[5] J.R. Matthews, J. Chem. Soc., Faraday Trans. II 83 (Part 7) (1987) 1273.
[6] C. Sari, U. Benedict, H. Blank, J. Nucl. Mater. 35 (3) (1970) 267.
[7] R.M. Harker, J. Alloys Compd. 426 (1–2) (2006) 106, doi:10.1016/j.jallcom.2006.02.014.
[8] J.R. Petherbridge, T.B. Scott, J. Glascott, C. Younes, G.C. Allen, I. Findlay, J. Alloys Compd. 476 (1–2) (2009) 543, doi:10.1016/j.jallcom.2008.09.113.
[9] G.C. Allen, P.M. Tucker, R.A. Lewis, J. Chem. Soc., Faraday Trans. II 80 (Part 8) (1984) 991.
[10] G.C. Allen, J.C.H. Stevens, J. Chem. Soc., Faraday Trans. 84 (Part 1) (1988) 165.
[11] K. Tharmalingham, Philos. Mag. 23 (181) (1971) 199.
[12] C.R.A. Catlow, Proc. R. Soc. A 353 (1675) (1977) 533.
[13] C.R.A. Catlow, J. Nucl. Mater. 79 (2) (1979) 432.
[14] J.R. Walker, C.R.A. Catlow, J. Phys. C: Solid State Phys. 14 (32) (1981) L979.
[15] R.A. Jackson, A.D. Murray, C.R.A. Catlow, Physica B 131 (1–3) (1985) 136.
[16] R.A. Jackson, A.D. Murray, C.R.A. Catlow, Ann. Chim. Faraday 10 (3) (1985) 227.
[17] C.R.A. Catlow, J. Chem. Soc., Faraday Trans. II 83 (Part 7) (1987) 1065.
[18] R.A. Jackson, A.D. Murray, J.H. Harding, C.R.A. Catlow, Philos. Mag. A 53 (1) (1986) 27.
[19] J.H. Harding, J. Chem. Soc., Faraday Trans. II 83 (Part 7) (1987) 1177.
[20] R.A. Jackson, C.R.A. Catlow, A.D. Murray, J. Chem. Soc., Faraday Trans. II 83 (Part 7) (1987) 1171.
[21] M.S.D. Read, M.S. Islam, F. King, F.E. Hancock, J. Phys. Chem. B 103 (9) (1999) 1558.
[22] M.E.G. Valerio, R.A. Jackson, J.F. de Lima, J. Phys.: Condens. Matter 12 (35) (2000) 7727.
[23] J.D. Gale, Philos. Mag. B 73 (1) (1996) 3. Meeting on Interatomic Potentials, Oxford, England, July 4–5, 1994.
[24] B.G. Dick, A.W. Overhauser, Phys. Rev. 112 (1) (1958) 90.
[25] J.D. Gale, J. Chem. Soc., Faraday Trans. 93 (4) (1997) 629.
[26] J.D. Gale, A.L. Rohl, Mol. Simul. 29 (5) (2003) 291, doi:10.1080/0892702031000104887.
[27] J.D. Gale, Zeitschrift für Kristallographie 220 (5–6) (2005) 552.
[28] A.K. Cheetham, P. Day (Eds.), Solid State Chemistry: Techniques, Clarenden Press, Oxford, 1987.
[29] N.F. Mott, M.J. Littleton, J. Chem. Soc., Faraday Trans. II 85 (Part 5) (1989) 565.
[30] C.R.A. Catlow, J. Chem. Soc., Faraday Trans. II 85 (Part 5) (1989) 335.
[31] S.A. Barrett, A.J. Jacobson, B.C. Tofield, B.E.F. Fender, Acta Cryst. 38 (November) (1982) 2775.
[32] G. Dolling, R.A. Cowley, A.D.B. Woods, Canad. J. Phys. 43 (8) (1965) 1397.
[33] J.B. Wachtman, M.L. Wheat, H.J. Anderson, J.L. Bates, J. Nucl. Mater. 16 (1) (1965) 39.
[34] I.J. Fritz, J. Appl. Phys. 47 (10) (1976) 4353.
[35] J. Schoenes, Phys. Rep. 63 (6) (1980) 301.
[36] A. Padel, C. Denovion, J. Nucl. Mater. 33 (1) (1969) 40.
[37] M.O. Marlowe, J. Nucl. Mater. 33 (2) (1969) 242.
[38] M. Abramowski, R.W. Grimes, S. Owens, J. Nucl. Mater. 275 (1) (1999) 12.
[39] B. Vessal, M. Amini, D. Fincham, C.R.A. Catlow, Philos. Mag. B 60 (6) (1989) 753.
[40] B. Vessal, M. Amini, C.R.A. Catlow, J. Non-Cryst. Solid 159 (1–2) (1993) 184.
[41] R. Winter, An Introduction to Some Key Concepts of Shock Hydrodynamics, AWE report 646/03.
[42] J.E. Hanlon, A.W. Lawson, Phys. Rev. 113 (2) (1959) 472.
[43] A.D.B. Woods, W. Cochran, B.N. Brockhouse, Phys. Rev. 119 (3) (1960) 980.
[44] J.D. Axe, G.D. Pettit, Phys. Rev. 151 (2) (1966) 676.
[45] R.H. Lyddane, R.G. Sachs, E. Teller, Phys. Rev. 59 (8) (1941) 673.
[46] M.T. Hutchings, J. Chem. Soc., Faraday Trans. II 83 (Part 7) (1987) 1083.
[47] K. Clausen, W. Hayes, M.T. Hutchings, J.E. MacDonald, R. Osborn, P. Schnabel, Rev. Phys. Appl. 19 (9) (1984) 719.
[48] K. Clausen, W. Hayes, J.E. MacDonald, R. Osborn, M.T. Hutchings, Phys. Rev. Lett. 52 (14) (1984) 1238–1241.
[49] K.N. Clausen, M.A. Hackett, W. Hayes, S. Hull, M.T. Hutchings, J.E. MacDonald, K.A. McEwen, R. Osborn, U. Steigenberger, Physica B 156 (1989) 103.
[50] H. Matzke, J. Chem. Soc., Faraday Trans. II 83 (Part 7) (1987) 1121.
[51] K.C. Kim, D.R. Olander, J. Nucl. Mater. 102 (1–2) (1981) 192.
[52] R. Szwarc, J. Phys. Chem. Solids 30 (3) (1969) 705.
[53] F.A. Kröger, H.J. Vink, in: F. Seitz, D. Turnball (Eds.), Solid State Physics, vol. 3, Academic Press, New York, 1956.